Lab on a Chip

CRITICAL REVIEW

View Article Online
View Journal | View Issue

Cite this: *Lab Chip*, 2025, **25**, 4273

Microfluidics for geosciences: metrological developments and future challenges

Sophie Roman, *[a] Flore Rembert, [ab] Anthony R. Kovscek [c] and Jenna Poonoosamy *[d]

This review addresses the main metrological developments over the past decade for microfluidics applied to geosciences. Microfluidic experiments for geosciences seek to decipher the complex interplay between coupled, multiphase, and reactive processes in geological porous media, *e.g.*, for groundwater management, soil remediation, gas storage in geological reservoirs, or geothermal energy. The guiding principle is to represent natural or engineered processes in a controlled environment to observe, characterize, and model them. When microfluidic experiments are associated with advanced metrology techniques, they provide direct visualization of the processes and measurements of transport mechanisms, chemical reactions, interfacial processes, or mixing within the pore space. In this review, we present the state of the art in metrological approaches to microfluidics for geosciences, including measuring velocity fields, fluid and solute saturations, tracking chemical reactions, and combining experimental and computational microfluidics. The upscaling from microfluidics to the reservoir scale is discussed. Finally, we outline future challenges related to metrological advancements and the integration of artificial intelligence in microfluidics.

Received 30th January 2025,
Accepted 22nd July 2025

DOI: 10.1039/d5lc00108k

rsc.li/loc

[a] *Univ. Orléans, CNRS, BRGM, ISTO, UMR 7327, F-45071 Orléans, France. E-mail: sophie.roman@univ-orleans.fr*
[b] *Department of Geology, Ghent University, 9000 Gent, Belgium*
[c] *Department of Energy Science and Engineering, Stanford University, 367 Panama Mall, 94305 Stanford, USA*
[d] *Nukleare Entsorgung (IFN-2), Institute of Fusion Energy and Nuclear Waste Management, Forschungszentrum Jülich GmbH, 52428 Jülich, Germany. E-mail: j.poonoosamy@fz-juelich.de*

1 Introduction

This review focuses on recent metrological developments in microfluidics, specifically as they apply to geosciences. Microfluidics refers to the manipulation of small volumes of fluids within channels typically measuring tens of micrometers.[1] Among the first applications of microfluidics was

Sophie Roman

Sophie Roman is an Associate Professor at the University of Orléans (France) and a member of the Institut des Sciences de la Terre d'Orléans (ISTO). She leads the Nanoμlab, a state-of-the-art micro-nanofluidic facility dedicated to exploring coupled processes in porous media. Roman is a microfluidic experimentalist driven by a fascination for the intricate interplay between flow microdynamics, geochemistry, and living systems in porous environments. Her research aims to enhance the estimation of storage capacity in geological reservoirs, minimize the footprint needed for CO_2 sequestration, evaluate the long-term behavior of stored CO_2, and accelerate the remediation of contaminated aquifers.

Flore Rembert

Flore Rembert is a Geophysicist specializing in geoelectrical methods. She focuses on monitoring the dynamic and reactive processes of the critical zone at multiple scales. Rembert has pioneered geoelectrical acquisition on a chip for reactive transport applications. She also develops petrophysical models. Coupled with reactive transport simulations, these theoretical advances provide new mechanistic insights into the measured geoelectrical signals for further field applications of geoelectrical monitoring. In 2024, Rembert was awarded a Senior Postdoctoral Fellowship at Ghent University (Belgium) for her research project on developing geoelectrical monitoring for PFAS contamination and remediation in the subsurface.

the characterization and quantification of multiphase oil and water flow in rocks, including the effects of surface wettability.[2] In the 1980s, microfluidics revolutionized the field of biotechnologies, *e.g.*, by miniaturizing chromatography processes to manipulate DNA or proteins.[3]

The use of microfluidic devices in the field of geosciences has expanded greatly since the 2010's to mimic and study transport processes in soil and subsurface microstructures. These devices are then called micromodels,[2] aquifer-on-a-chip, or geological-lab-on-a-chip. The idea is to represent natural or engineered processes in a controlled environment, observe them under a microscope, and characterize and model them.

The need for pore-scale studies in geosciences arises because aquifers and subsurface formations are opaque porous reservoirs where the typical pore size is on the order of tens of micrometers. Analyzing transport processes at the pore scale is essential to decipher complex coupled mechanisms of subsurface flows, *e.g.*, underground repositories for nuclear waste,[4] CO_2 sequestration,[5] geothermal energy extraction,[6] and environmental remediation.[7]

Obtaining details about the interaction among flow, geochemical reactions, and colloid transport serves to predict the evolution of subsurface reservoirs and to control engineered processes. For example, the process of CO_2 storage involves the injection of CO_2 into a deep geological reservoir of porous rock where it displaces native fluid (typically brine) from pore spaces. The effective CO_2 storage capacity worldwide is uncertain because the influence of complex coupled processes occurring during and after injection is often neglected.[8] Indeed, the current macroscale models that describe multiphase flow and the transport of species miss important physicochemical processes.[9,10] Thus, a classic strategy to derive macroscale models rooted in elementary physical principles involves investigating the pore-scale processes where the physics is better understood before they are upscaled to the reservoir scale. Underground hydrogen storage is one of the recent options for low-carbon energy transitions. Accurate modeling of hydrogen storage at lab and pilot scales requires a solid understanding of flow and trapping phenomena in porous media.[11,12] Dedicated microfluidics experiments need to account for the highly diffusive behaviour of hydrogen and high-pressure conditions of the storage while ensuring safe and reliable experimentations.

The recent and accelerating improvements in microfluidics, imaging techniques, and high-performance computing offer new possibilities to decipher and quantify the mechanisms leading to gas storage in geological reservoirs, see *e.g.*[13–18] Another example of microfluidics for geosciences is the modeling of reactive transport processes that include dissolution and precipitation of minerals and their effects on flow and rock properties[19–27] and contaminant transport including radionuclides.[28]

Microfluidics also holds great promise for environmental remediation purposes, setting new frontiers in radio-geochemistry by enabling access to critical information, such as crystallization kinetics of highly radioactive substances (*e.g.*, Ra-bearing minerals), while minimizing radioactive exposure.[28]

Comprehensive reviews have already been published on the use of microfluidics to investigate key pore-scale processes involved in CO_2 underground storage,[29–31] on microfluidic applications for studying oil extraction and recovery processes,[32] on the role of microfluidics in addressing challenges associated with the transition to a low-carbon future,[6] and on the use of micromodels for two-phase flow studies.[33] Additionally, critical reviews summarizing advances in micromodel fabrication and imaging techniques for geosciences are available.[34,35] In this review, we specifically focus on metrological developments in

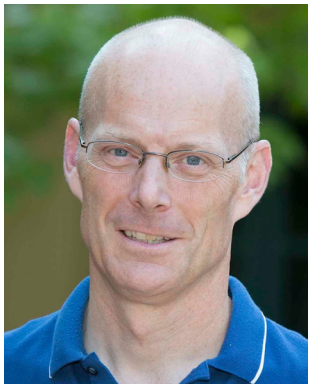

Anthony R. Kovscek

Tony Kovscek is the Keleen and Carlton Beal Professor at Stanford University. He codirects the Stanford University Energy Transition Research Institute (SUETRI-A) and the Stanford Center for Carbon Storage. Kovscek and his research group seek to understand the complex multiphase flows in porous media that are the basis for sustainable subsurface engineering. He is a member of the U.S. National Academy of Engineering and was honored to receive the John Franklin Carll Award, the Lester C. Uren Award, and the Distinguished Achievement Award for Faculty from the Society of Petroleum Engineers.

Jenna Poonoosamy

Jenna Poonoosamy is a Research Scientist at Forschungszentrum Jülich (Germany), where she leads the Reactive Transport group at the Institute of Fusion Energy and Nuclear Waste Management. Her research focuses on using microfluidic platforms to study geochemical processes at the pore scale. She has designed state-of-the-art microfluidic experiments to investigate the crystallization of Ra-bearing minerals, contributing to a better understanding of radionuclide behavior in the environment. Her work integrates in situ Raman spectroscopy with geochemical and reactive transport modeling to examine mineral nucleation, growth, and coupled transport-reaction mechanisms. These studies support applications in energy and subsurface systems.

microfluidics that enable more advanced and quantitative characterization of pore-scale processes.

Micromodels are two-dimensional representations of the pore space that are etched or molded on a substrate by photolithography methods and then covered by a transparent material. The etched pattern may be of variable complexity depending on the research objective. Single microchannels are used to focus on one phenomenon while isolating the others.[10,36] More complex patterns that consider the heterogeneity and microstructure of a porous medium are representative of natural porous media.[37–39] Real rock micromodels[40–42] allow representation of chemical compositions and reactions found in the subsurface. Because micromodels are two-dimensional representations of porous media, the upscaling of their flow and transport properties to three-dimensional reservoir rock should be made with caution. Therefore, microfluidic experiments can be complemented with numerical models, or with core-scale experiments to provide data to verify and complete models, and to improve large-scale models.[20,43–46]

To confront micromodel experiments with theory, numerical or column-scale predictions, quantitative data on the flow, transport, and chemical processes are needed. The parameters of interest to monitor in high-resolution and real-time are the velocity of the fluids, displacement of interfaces (fluid–fluid, fluid–solid), saturations, chemical compositions, and trajectory of colloids. For example, the formation of colloidal or biofilm aggregates is monitored to assess their consequence on flow, transport, and storage properties.[47–49] For such needs, metrological developments are necessary to stay at the frontier of measurement capabilities. This review aims to introduce recent developments that go beyond the state of the art developed for microfluidics for geosciences and highlight the upcoming challenges. First, we introduce the basis of microfluidic setups. Then, we present the main metrological developments of the last ten years, focusing on measuring fluid occupancy and velocity fields, tracking chemical reactions, and scaling up microfluidics data to larger scales. The last section highlights the future challenges.

2 Materials and imaging

In this section, we introduce micromodel properties: geometry, materials, and wettability. Next, we briefly introduce the imaging methods to obtain sequences of images of the physicochemical processes within micromodels. Then, we present the common image processing and analysis methods.

2.1 Micromodel properties

Micromodels are of various geometries depending on the objective of the research that is conducted, see Fig. 1. Simple geometries, such as a straight microchannel containing one pore or a succession of pores, are used to isolate and probe processes in controlled environments,[10,36,50,51] or understand bubble flow in capillaries.[52] Geometries representative of the pore size and shape of subsurface environments are obtained by imaging a rock thin section.[37,53] Real minerals can be incorporated[20,54] or precipitated[55,56] inside microchannels to replicate geochemical environments for further investigations. For a better representation of reservoir rock properties, micromodels can be functionalized by coating the inner surfaces of the channels with geomaterials.[21,57,58] Finally, micromodels can be made from real-rock samples.[19,40,41,59,60]

Different materials can be used to fabricate micromodels, each with advantages and drawbacks. Silicon-etched micromodels covered by a glass plate allow for high-fidelity reproducibility of patterns, even those with sub-micrometric dimensions, and they are highly chemically resistant.[61] One side of the micromodel, however, is not transparent, and etching techniques are time-consuming and expensive. Silicon-etched micromodels do have advantages in attaining relatively high pressure (10's to 100's bar) either through refinements in the design and fabrication processes[62,63] or placing the relatively stiff micromodel in a pressure vessel

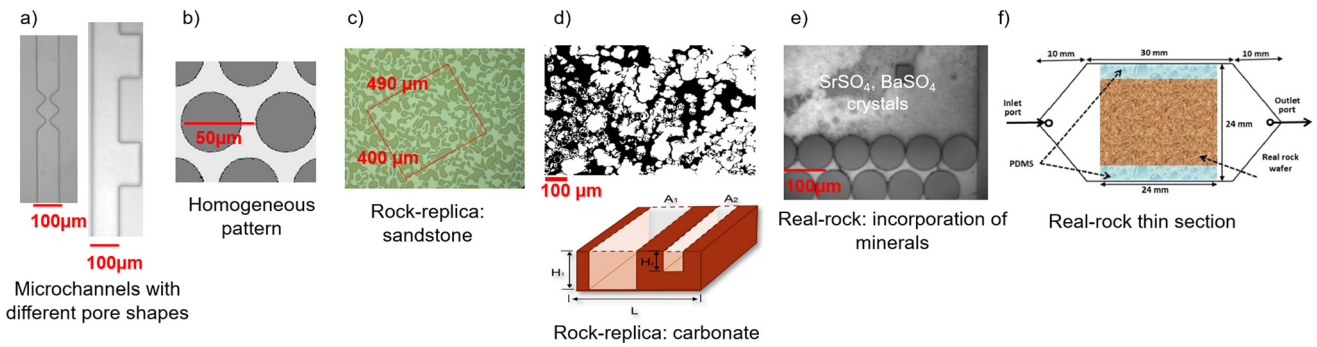

Fig. 1 Diversity and complexity of micromodels for geosciences. Micromodels are a two-dimensional representation of a porous medium that allows for direct visualization of pore-scale mechanisms. A pattern is etched into a substrate and covered by a transparent cover plate. a) Single pores, *e.g.* Roman *et al.*,[10] b) cylindrical pillars homogeneously distributed, *e.g.*, Roman *et al.*,[15] c) and d) geometries drawn from images of real rocks with 1 : 1 representation of pore sizes, c) a sandstone, *e.g.* Buchgraber *et al.*,[37] d) a carbonate with two different etching depths to differentiate micropores and macropores, reproduced from Yun *et al.*[38] with permission from Royal Society of Chemistry, copyright 2017, e) microfluidic reservoir filled with minerals, *e.g.*, Poonoosamy *et al.*,[54] f) real rock-microfluidic flow cell, reproduced from Singh *et al.*[19] with permission from Elsevier, copyright 2017.

that reduces the differential stress across micromodel boundaries.[37,61]

Glass micromodels have the advantage of being transparent and chemically resistant. The wet-etching technique, generally used for glass microfabrication, has limitations on the minimum reachable pore sizes and produces trapezoidal cross-sections. Microfabrication by PDMS (polydimethylsiloxane, a silicone polymer) molding is widely used in microfluidics.[64] Microfabrication in PDMS is simple, cheap, and allows for the replication of complex porous media patterns of micrometric pore sizes. PDMS is transparent, and the effect of light refraction on the walls is less pronounced than for glass microchannels. PDMS, however, is permeable to gases and solvents, that makes it not suitable for some experiments. In addition, PDMS is a soft material. Thus, it is not representative of the mechanical properties of real rocks. Another low-cost solution is 3D printing, also called stereolithography, a method where the object is created by adding successive layers of material.

The materials used for the fabrication of 3D-printed objects are varied (plastic, wax, metals, glass, and so on). For now, the minimum pore sizes obtained by 3D printing (about 100 μm) are well above the resolution of microfabrication techniques. Moreover, the accuracy of current printers generates an uncontrolled roughness on the surface of the porous structure that is likely to artificially destabilize the flows in these micromodels.[65] Nevertheless, the rapid progress of this technique suggests that it could compete with microfabrication within a few years. Complete reviews on the materials and fabrication methods to make porous system micromodels are presented in Anbari *et al.*,[34] Gerami *et al.*[66]

A key aspect in studying subsurface processes is experiments under pressure and temperature conditions representative of deep geological environments, giving information on reactive flows, mineral reactions, and (bio) geochemical processes. For example, underground gas storage processes (CO_2, H_2) can be studied using silicon-Pyrex micromodels under conditions reaching pressures up to 300 bars and temperatures of 400 °C.[29,67] Ultra-high pressure micromodels are being developed for applications such as geothermal energy storage, deep CO_2 geological storage, or studying the deep underground biosphere.[68] Additionally, micromodels with specialized high-pressure holders are used to understand the trapping and dissolution of supercritical CO_2.[69] Recent advances have made it possible to fabricate full-sapphire microreactors that can withstand pressures of up to 800 bars,[70] enabling investigations across a wide range of experimental conditions.

Controlling the wettability of the surfaces of microfluidic devices is of particular interest because of the impact on transport properties (imbibition, drainage, trapping, remobilization, particle/wall interactions, and so on). The different materials used in microfluidics result in different wettability properties. Glass and silicon micromodels are water-wet, with contact angles between the surface, water, and air below 60°. Propagating an atmospheric pressure plasma directly into a glass microdevice produces highly hydrophilic properties that remain stable for long periods.[71] PDMS has a heterogeneous hydrophobic nature and, thus, it is usually treated to ensure a homogeneous hydrophilic or hydrophobic wettability.[72–74] Exposure of a PDMS micromodel to plasma treatment in a plasma reactor for 5 minutes allows the surface to remain hydrophilic for more than 6 hours.[75] PDMS with a hydrophilic surface can also be obtained *via* the deposition of polyvinyl alcohol following the protocol of Trantidou *et al.*[74] PDMS with a homogeneous hydrophobic surface can be obtained by silane deposition following Karadimitriou *et al.*[73] Moreover, some resins (*e.g.*, NOA81) allow for wettability control over a wide range of contact angles.[76]

One of the key challenges in representing subsurface conditions is accurately accounting for the mixed-wettability of rocks.[77] Mixed wettability arises when hydrophobic components, such as crude-oil asphaltenes, adhere to pore surfaces devoid of protective aqueous films.[78] In mixed-wet pores, hydrophobic and hydrophilic surfaces coexist. With crude-oil/water systems, it is relatively straightforward to obtain a degree of mixed wettability in micromodels due to the propensity for crude-oil components to sorb to pore walls while pore corners and pendular rings retain bulk aqueous fluids.[79] Additionally, Chang *et al.*[80] created mixed-wet surface properties by applying a heterogeneous flow of octadecyltrichlorosilane. Bespoke localisation of wettability patterns can be obtained by soft lithography combined with thin film deposition,[81] or by plasma enhanced chemical vapor deposition using a precursor that reduces the wettability.[82]

2.2 Image acquisition and processing

Imaging. To record the processes within micromodels, direct visualization with a camera is used when magnification of the images is not necessary. More often, a micromodel is placed under a microscope connected to a camera. Depending on the resolution and field of view needed, different objective lenses with a specific magnification and numerical aperture are used. The image pixel size typically ranges from tens of nanometers to tens of micrometers. Optical microscopes use visible light to generate magnified images. Fluorescent microscopy uses fluorescence to obtain images. In this case, the micromodel is illuminated with light of a specific wavelength that is absorbed by fluorescent chemical compounds, causing them to emit light of different wavelengths. Confocal microscopy enables the capture of multiple two-dimensional images at different depths, allowing for the reconstruction of three-dimensional images of the micromodel. More detailed reviews of imaging methods are found in Karadimitriou and Hassanizadeh,[33] Jahanbakhsh *et al.*[35]

Image processing and analysis. Image processing techniques treat an image as a two-dimensional signal and apply signal processing techniques to improve image quality and extract information. The purpose of image processing is usually to make apparent or to hide elements in an image for

further analysis (quantification, tracking). First, the quality of image acquisition is crucial. Then, image processing techniques[83] may be applied to images to count objects, measure the saturation of fluid phases, track fluid–fluid or fluid–solid interfaces, track particles, and so on.[12,15,20,60]

3 Methodological developments

In this section, we describe the latest developments dedicated to metrological advancements for microfluidics in geosciences. Several parameters usually need to be measured or tracked during micromodel experiments. For example, it is useful to obtain the fluid saturations and track the displacement of a fluid–fluid interface to characterize flow regimes during two-phase immiscible flow experiments.[73,84,85] The study of colloids leads to the need to track colloidal particles or to characterize colloid aggregates,[47] *e.g.*, to assess the mechanisms of pore-clogging by particles in porous media. Understanding hydrogeochemical couplings requires tracking chemical reactions.[20,40] We start this section by discussing methods to measure fluid distributions, velocity fields, concentration fields, reactive fronts, mineral reactions, biofilms, and bioreactions. The next section is dedicated to the combination of microfluidics with numerical methods to augment experimental data. Then, we discuss the techniques for macroscale interpretation of microfluidic data.

3.1 Measuring fluid saturations and flow paths

During immiscible two-phase flow in porous media, measuring pore-saturation levels and interfacial area is critical to evaluate the efficiency of the displacement process. The fluid saturation is the fraction of the pore volume occupied by one of the fluids (water, air, CO_2, oil, non-aqueous phase liquid, and so on). The interfacial area is the area of contact between the fluids. Flow regimes are characterized by the viscosity ratio M (viscosity of the advancing fluid divided by the viscosity of the displaced fluid), and the capillary number Ca (ratio of viscous forces over surface tension).[85,86]

Fluid–fluid distribution is classically determined through optical imaging of micromodels. Fluids are differentiated using dyes, fluorescent or not. Saturation is measured through image processing from the top view of the micromodel. When a fluorescent dye is used, the saturation is directly determined from the fluorescence intensity captured by a camera,[85,87] see Fig. 2. The specific interfacial area between two fluids can also be determined from images of fluid distributions.[88] The spatial and temporal resolution of the image acquisition depends on the dimensions of the porous pattern and the need for dynamic measurements.[33] Challenges lie rather in the precision of the measurements. In particular, measurements from the top view of the micromodel usually assume a 2D representation of fluid saturations, as in Fig. 2a and b. Both fluid phases, however, are often present in the vertical cross-section of the pores, due to wetting films coating the solid grains. Therefore, measuring fluid saturation along the vertical direction is highly valuable but can be challenging.

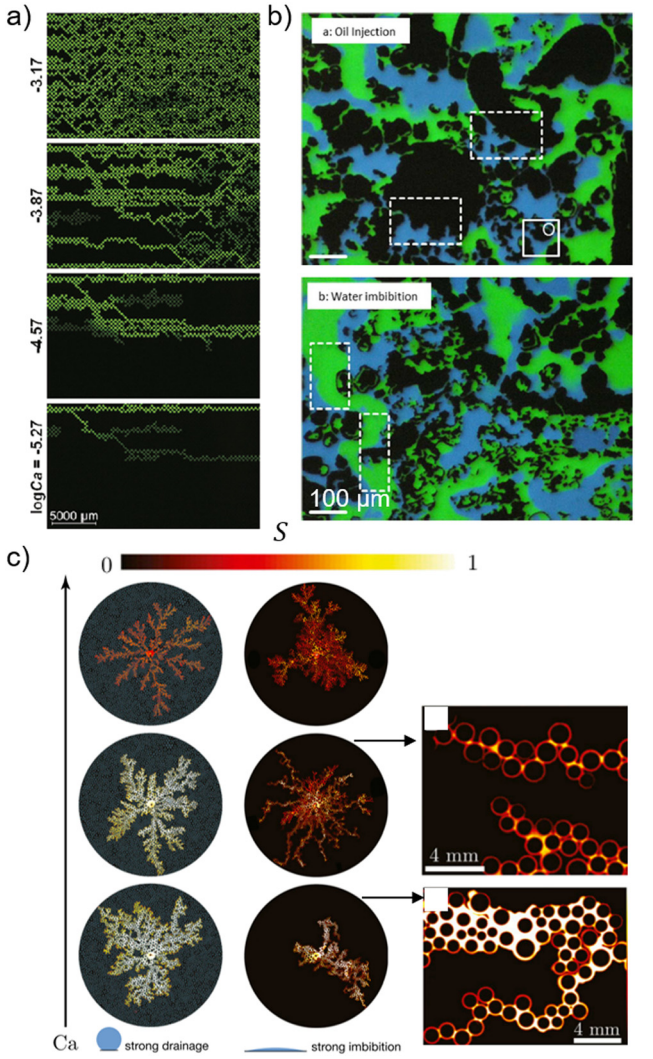

Fig. 2 Fluid saturations in micromodels. a) Macroscale images of a non-wetting phase (green) displacing a wetting phase (black) for a viscosity ratio $\log M = -1.95$ and different values of capillary number. The micromodel is made of a uniform distribution of cylindrical pillars (in black, 300 µm in diameter), reproduced from Zhang *et al.*[85] with permission from American Chemical Society, copyright 2011. b) Images of oil injection and water injection in a micromodel representative of a carbonate rock. The grains are black, water is green, and oil is blue, reproduced from Yun *et al.*[38] with permission from Royal Society of Chemistry, copyright 2017. c) Patterns of displacement of silicone oil by water at unfavorable viscosity ratio, for strong drainage (θ = 150°) and strong imbibition (θ = 7°). The circular microfluidic cell (diameter of 10 cm) with radial injection is made of cylindrical pillars of different sizes. Capillary numbers from top to bottom are Ca = 2.9×10^{-3}, 2.9×10^{-2}, 2.9×10^{-1}. The color indicates the saturation of the invading wetting phase in the depth of the micromodel. On the right, snapshots from strong imbibition are presented, showing invasion by corner flows. The wetting phase coats the contours of the posts and does not fill the pore space. Liquid wedges in corners can swell and expand over time. Reproduced from Zhao *et al.*[76] with permission from National Academy of Sciences, copyright 2016.

For saturations in the vertical direction, Zhao *et al.*[76] used a light-absorbing dye and generated a calibration curve that relates the transmitted light intensity to the dye concentration

in the wetting phase. Then, they convert the transmitted light intensity to water saturation in the depth of the microfluidic cell. Therefore, in addition to the 2D fluid distribution (Fig. 2a and b), an indication of the depth-saturation is provided (Fig. 2c). Using this method, Zhao *et al.*[76] show that the invasion happens through corner flows for some conditions, see snapshots in Fig. 2c.

The principle of measuring fluid saturations in the depth of microchannels by optical photometric techniques is presented in Fig. 3.[50] A capillary, or microchannel, is saturated with a wetting fluid seeded with a light-absorbing dye (fluorescent or not), then a non-wetting fluid is injected (*e.g.*, air). Optical photometric techniques rely on relating a measure of the optical density in a channel to the dye concentration. For that, the light attenuation at any point (x, y) in an image of a channel is defined as the ratio $I_0(x, y)/I(x, y)$, where I_0 is an image of the empty channel and I is the image of the channel filled with fluids. The optical density is then defined as follows, $\mathrm{OD}(x, y) = \log(I_0(x, y)/I(x, y))$, and measured pixel by pixel. Classically, OD is related to the concentration using a calibration curve for known concentrations.[89,90] The technique can be extended to the measure of liquid-film thickness.[50]

In Fig. 3 we present the validation of the method when the motion of air bubbles in a straight tube is considered where numerical data were available and the theory of Bretherton[91] gives the relation between the liquid-film thickness and the capillary number. Later, the technique was used to determine and compare the dynamics of film thickness at a pore constriction during snap-off events (*i.e.*, the detachment of a gas bubble during drainage) with numerical modeling. The main advantages of the technique are that it is non-intrusive, inexpensive, very easy to implement, has good accuracy, and allows for dynamic measurements as in Roman *et al.*,[50] Zhao *et al.*[76]

The primary advantage of the optical methods presented is their non-intrusive nature, allowing flow processes to be observed without disturbance. Limitations in fluid saturation measurements are mainly related to the spatial and temporal resolution of image acquisition. Advances in microscopy and high-resolution cameras now enable high-speed imaging with sub-micrometer resolution, significantly enhancing the ability to capture rapid, small-scale processes.

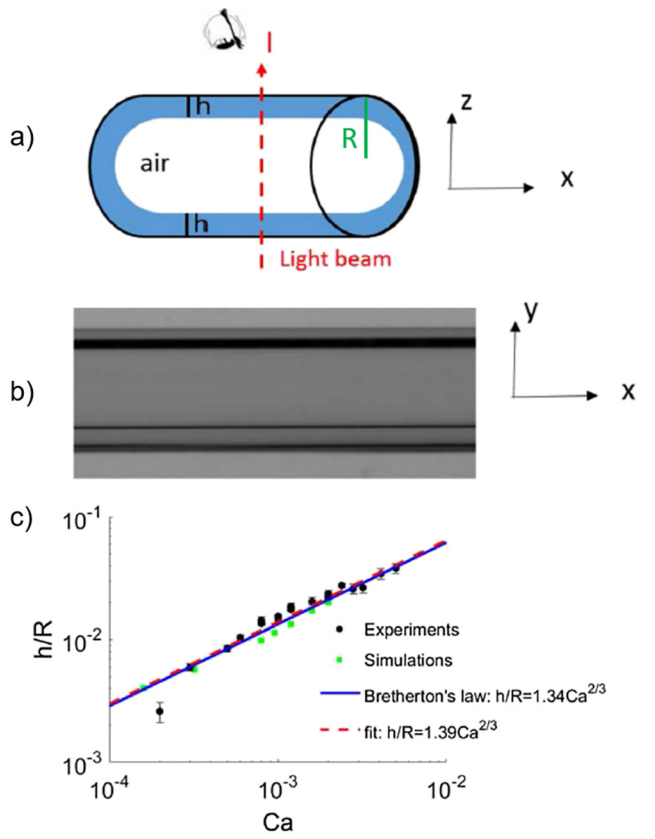

Fig. 3 Principle of measuring the fluid saturation in the vertical direction. a) Schematic of wetting films of thickness h along a tube wall. b) Grayscale image of the films. c) Validation of the film thickness measurements. Averaged film thickness normalized by the tube radius for different capillary numbers: experiments (black dots), numerical data (green squares), fit of the experimental data (red dashed line), and Bretherton's theory (blue line). Reproduced from Roman *et al.*[50] with permission from Elsevier, copyright 2017.

3.2 Measuring velocity fields during microfluidic experiments

A detailed understanding of the underlying physics of flow and transport in geological porous media is of great importance. Knowledge of fluid saturations (see previous section) is essential but not always sufficient. An analysis of velocity fields is particularly useful to assess pore-scale mechanisms and their consequences and to compare quantitatively experiments with theoretical or numerical data. The particle tracking velocimetry (PTV) and particle image velocimetry (PIV) techniques are optical methods of flow visualization based on the detection of tracer particles in the flow field. Successive experimental images are recorded and analyzed through particle tracking (PTV) or spatial correlation (PIV) methods. Peurrung *et al.*[92] introduced PTV to measure porous medium velocity fields within a packed bed of transparent spherical beads. Santiago *et al.*[93] introduced micro-particle image velocimetry (micro-PIV) that uses a microscope, micron-sized particles, and a high-resolution camera to record particle-image fields. Velocity field measurements in complex porous geometries, such as pore networks or realistic geological porous medium replicas, have only been available for a few years.

Principle of micro-PIV. The principle of micro-PIV is presented in Fig. 4. The fluid is seeded with micron-size particles, these particles are chosen so that they follow the flow without disturbing it.[94] Most micro-PIV systems use fluorescent tracer particles, a laser, an epifluorescent microscope, a high-speed camera for observation, and optical filters to block non-fluorescent light disturbances. Optical images of non-fluorescent particles can also be used and followed by image processing to obtain images containing information only related to the moving particles,[15] see Fig. 5. The velocity field is

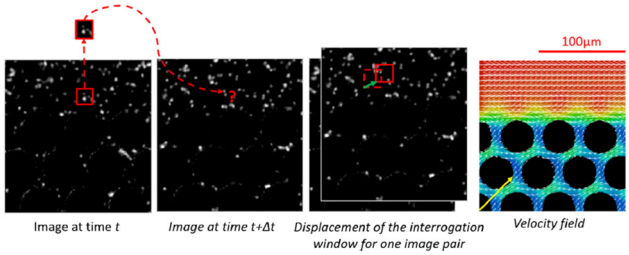

Fig. 4 The principle of PIV is to record two images of the flow of particles separated by a short time delay Δt. Images are subdivided into many small interrogation windows. The displacements of interrogation windows between two images are determined through spatial cross-correlation. Velocity is merely found by dividing the particle displacements by the time between images. Time averaging is performed over at least 10 image pairs to obtain the distribution of velocity fields. Reproduced from Roman *et al.*[15] with permission from Elsevier, copyright 2016.

calculated by cross-correlating interrogation windows between two successive images of a sequence, see Fig. 4. The parameters of the optical system, of the particles, and for PIV analysis must be chosen carefully to ensure that the measured velocities are representative of the actual velocity of the fluid.[94] Several tools are available to implement PIV analysis. For example, PIVlab is a widely used, powerful, and open-source software.[95]

Micro-PIV for complex porous media geometries. In microfluidic devices representative of geological porous media, Roman *et al.*[15] compared micro-PIV results with numerical simulation of single-phase flow for which the dynamical models are well understood and serve as a tool to validate the experimental measurements. In Fig. 5, velocity fields and velocity profiles obtained experimentally and numerically are shown. By optimizing micro-PIV parameters, a very good agreement is obtained between experiments and simulations.

Micro-PIV measurements can be performed in micromodels with pore sizes below 10 μm and with a vector resolution of about 1 μm.[15,96] Micro-PIV was instrumental in understanding the difference in velocity fields between single-etch-depth micromodels and those where smaller pore spaces are etched less deeply compared to larger pore spaces.[38] Dual-depth etching is thought to produce a more realistic pore network.

Tracking velocity fields of two fluid phases. Using micro-PIV, it is possible to seed two fluid phases with different particles to follow the behaviour of each fluid. For example, using spectral separation, Blois *et al.*[96] used two cameras to image two immiscible fluids separately. Heshmati and Piri[97] introduced a two-phase and two-fields-of-view micro-PIV system to study simultaneously flow fields at the pore scale and the whole micromodel scale. They use this system to understand the distribution of fluid during two-phase immiscible flows and shear stress at the fluid–fluid interfaces, see Fig. 6.

Micro-PIV to record 3-dimensional velocity fields. Most micro-PIV setups are used to record 2D velocity profiles from the top view of a micromodel. Indeed, microfluidic devices are assumed to be two-dimensional, and velocities are measured for only one focal plane that corresponds to the whole thickness.[15] During micromodel experiments, out-of-focus particles appear in the recorded images. The particles in focus appear as small, well-defined bright dots, whereas the particles that are slightly out of focus are larger and blurred. Image pre-processing can be performed to highlight particles in focus (*i.e.*, in the plane of measurement) and to remove poorly resolved particles.[98]

Measurements at different focal planes are useful for obtaining the distribution of velocity fields in the depth of a microfluidic device.[99,100] However, the different planes are recorded at different times. Light field micro-PIV allows recording of instantaneous 3-dimensional velocity measurements.[101,102]

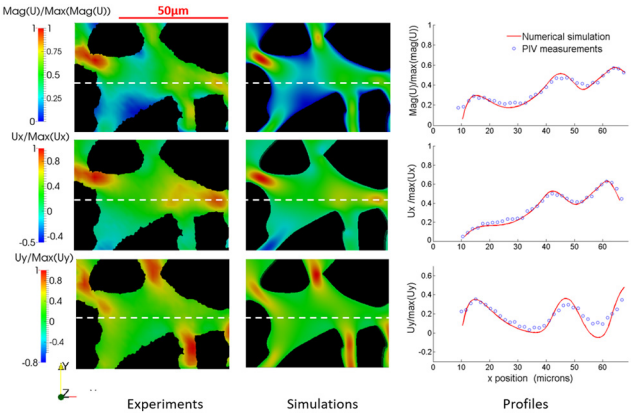

Fig. 5 Single-phase flow in a sandstone micromodel geometry. Comparison of velocity distributions between micro-PIV measurements and numerical results. Velocity profiles plotted along the white dotted line are also compared. Here, the experimental vector resolution is 1.76 μm × 1.76 μm. Reproduced from Roman *et al.*[15] with permission from Elsevier, copyright 2016.

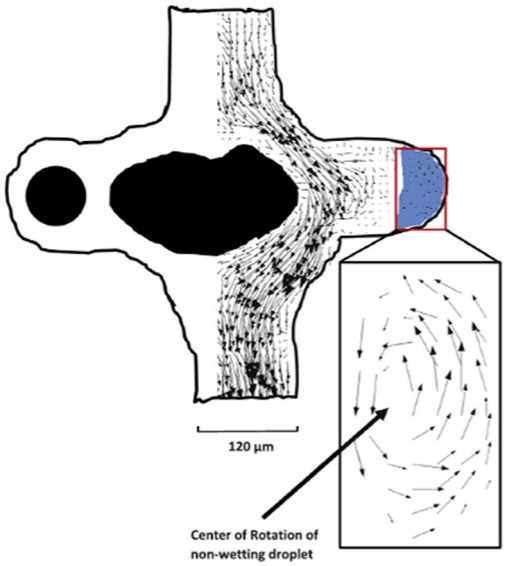

Fig. 6 Velocity fields obtained by micro-PIV in both invading wetting and trapped non-wetting phases. Reproduced from Heshmati and Piri[97] with permission from Elsevier, copyright 2018.

Light-field micro-PIV tracks the spatial positions of the particles in the flow. The position of the particle in the depth of the device is reconstructed based on the appearance of the particle that changes with the distance of focus.

Micro-PIV to unravel subsurface processes. Efforts toward PIV analysis of immiscible two-phase flow in micromodels have shown interesting behaviors.[15,17,103] Unsteady velocity events were associated with pore-scale events such as Haines jumps (sudden jumps of the fluid interface linked with fluid redistribution).[15,103] Interestingly, observation of dissipative events was made possible by the use of micro-PIV. After the passage of the fluid interface, clusters of the wetting phase remain trapped in the asperities of a rock replica micromodel, see Fig. 7a. This residual saturation is not immobile. This observation is contrary to what is commonly accepted; instead, recirculating motion is observed.[10,15] Fig. 7a shows streamlines computed from micro-PIV for one trapped water cluster during oil injection. Kazemifar *et al.*[103] observed shear-induced circulation zones within trapped water ganglia when supercritical CO_2 is injected, see Fig. 7b. It is usually accepted that the viscous-driven effect of one fluid on the other is negligible at a larger scale. Therefore, micro-PIV provides new elements to characterize dissipative events in porous media[10] that might have a significant impact on CO_2 trapping and fate during geological CO_2 storage.

Micro-PIV is a powerful and widely used technique for measuring velocity fields in microfluidic systems. Its application to multiphase flow in porous media presents some limitations. Optical distortions caused by multiple fluid interfaces, light scattering, and refractive index mismatches between the fluids and the solid matrix can significantly degrade image quality and measurement accuracy. Additionally, tracer particle seeding is complicated in multiphase systems, as particles may preferentially distribute within one phase or become trapped at interfaces. Despite these constraints, micro-PIV remains a valuable tool when combined with complementary techniques or adapted through index-matching and careful system design.

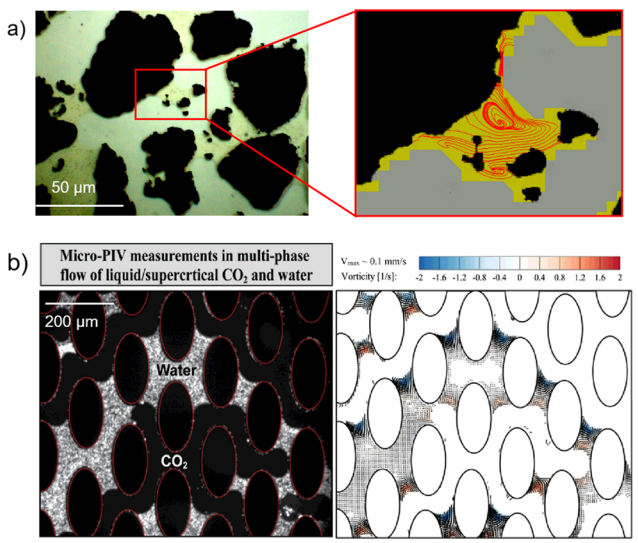

Fig. 7 Dissipative events during immiscible two-phase flows unraveled by micro-PIV. a) After the invasion, a pocket of water is trapped surrounded by solid grains and oil. From micro-PIV measurements, the streamlines are plotted and they show a recirculating motion of the trapped water, reproduced from Roman *et al.*[15] with permission from Elsevier, copyright 2016. b) Shear-induced circulation zone near the CO_2–water interfaces, reproduced from Kazemifar *et al.*[103] with permission from Elsevier, copyright 2016.

3.3 Tracking chemical reactions

This section is dedicated to measurement techniques to track chemical reactions during microfluidic experiments. It is important to characterize solute spreading, as solute mixing controls reaction rates for various processes.[90] In reactive transport modeling, one of the challenges is to develop process-based models that describe coupled processes with a realistic description of the effect of mineralogical reactions on transport properties of the rock matrix and further reaction rates.[104] First, we introduce recent methods to measure the concentration fields of species. Then, the use of chemiluminescence to characterize reactive fronts is presented. The last part is dedicated to tracking mineral reactions.

Concentration fields. Conservative tracers can be used to map concentration fields during micromodel experiments, *e.g.*, using fluorescein sodium salt solutions.[90] A fluorophore is a substance that absorbs light at a specific wavelength and emits light at another wavelength.[105] The amount of photons emitted is proportional to the number of excited tracer molecules and thus to the local tracer concentration. Using the characteristics of fluorophores, fluorescence microscopy enables specific visualizations. Multicolor images of several types of fluorophores can be composed by combining several one-color images. Using fluorescein, Borgman *et al.*[90] converted the light intensity of images to solute concentration based on a calibration curve. The magnitude of the concentration may then be calculated from the images. In this case, the two-dimensional concentration field averages the concentration field over the micromodel thickness. With this technique, Borgman *et al.*[90] demonstrated the role of pore-scale shear flow on concentration gradients, shedding light on the mechanisms driving mixing in porous media. Salek *et al.*[106] used fluorescein to investigate the effect of multiscale porosity on the evolution of the solute concentration field.

Measuring pH *in situ*. Measuring pH *in situ* during micromodel experiments is important for a number of geochemical processes. For example, during CO_2 injection in saline aquifers, part of the CO_2 dissolves into the brine, resulting in an acidified aqueous phase with some mineral dissolution or precipitation that can happen as a consequence.[107,108]

Chang *et al.*[18] studied the dynamic dissolution of supercritical CO_2 in an initially water-saturated rock-replica micromodel with the aim to image pH of residual water. They use a pH-sensitive fluorescent water dye with lower pH resulting in higher water intensity as visualized with a fluorescent

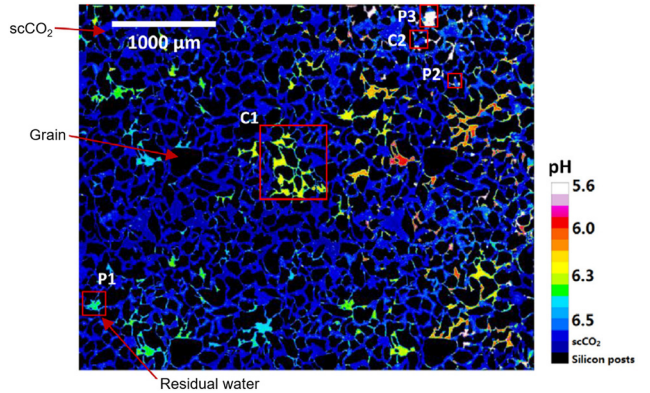

Fig. 8 Images of water pH interpreted from intensity values, $scCO_2$, and solid grains for 8455 pore volume of injected $scCO_2$. The flow direction is from left to right. Reproduced from Chang *et al.*[18] with permission from Elsevier, copyright 2017.

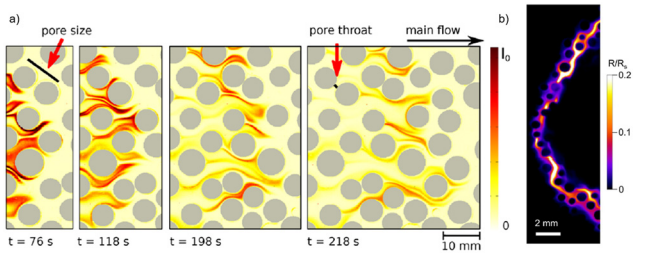

Fig. 9 a) Field of light intensity produced by cheminoluminescent reactions between reactants, reproduced from de Anna *et al.*[111] with permission from American Chemical Society, copyright 2014. b) Reaction rate fields for reactive transport experiment in a porous medium. The reaction rate is normalized by the reaction rate at which the image is saturated (the upper limit of the detection range). Reproduced from Izumoto *et al.*[112] with permission from John Wiley and Sons, copyright 2023.

microscope, see Fig. 8. The pH indicator pHrodo Red used in this study is functional for the pH range 4 to 9. A calibration is needed to relate the pH to the water intensity. They found that the lowest reliable pH level for the pHrodo Red dye was pH = 3.7. So far, no other pH-dependent dye has been described for microfluidic studies involving water and supercritical-CO_2.[18]

Instead of adding a dye to the fluid phase, microfluidic devices can be functionalized for pH mapping. For example, Florea *et al.*[109] integrated the pH optical capabilities based on polyaniline to microfluidic devices. The method allows spatial localization of pH gradients in micromodels over a wide range of pH (pH = 2–12). The setup includes a spectrophotometer and a camera to generate the pH estimations based on color measurements. Zhang *et al.*[110] also created a microfluidic porous medium coated with polyaniline for pH characterization. They compared experimental results with direct numerical simulations and found that the polyanaline coating provides real-time pH. This method allows visualization of dynamic pH changes relevant to the reactive transport of CO_2 during sequestration or for underground hydrogen storage.

Reactive fronts. Chemiluminescence is a useful technique for characterizing reactive fronts by mixing two reactants that emit light upon reaction. de Anna *et al.*[111] proposed a new experimental setup that uses micromodels and chemiluminescent reaction to quantify the rate of product formation for a bimolecular reaction, see Fig. 9. They can measure local concentration fields dynamically for a wide range of flow rates and local reaction rates within the micromodel. This setup allows quantifying the basic mechanisms that govern the mixing and reaction dynamics at the pore scale. Their setup, however, requires the use of a highly corrosive chemical compound.[111] Izumoto *et al.*[112] used luminol chemiluminescence, where blue light is emitted by the chemical reaction. The luminol chemiluminescence has the advantage of being safe and easy to handle. The reaction is approximated by,

$$A + B \rightarrow C + \text{photon}. \quad (1)$$

The chemiluminescence allows visualization of reaction rate fields for reactive transport experiments, see Fig. 9b, providing new insights into the dynamics of mixing and reactive fronts. Fluids of different chemical compositions that converge and react can be found in a large range of subsurface flows. Zhang *et al.*[110] used chemiluminescence to unravel the mechanisms controlling fluid–fluid reactions in two-phase flow in porous media.

Follow mineralogical reactions using Raman spectroscopy. The integration of microfluidics with confocal Raman spectroscopy[113,114] provides a robust platform for investigating geochemical processes and reactive transport phenomena. This approach enables *in situ* and non-destructive four-dimensional (4D) analyses of mineral reactivity and aqueous chemistry, offering high-resolution insights into the spatio-temporal evolution of chemical and pore structures within complex systems. The principle of Raman spectroscopy is to measure the vibrational modes of molecules to then identify molecules.[113] Raman coupled with microfluidics provides information on the fluid and mineral phases that are present. Thus, it allows for the identification of chemical pathways, to follow the displacement of species from the fluid into the solid phase or *vice versa*.

The lateral d_l and axial d_a resolution of Raman imaging are usually estimated from the theoretical diffraction limit given by $d_l \approx \frac{1.22\lambda}{NA}$ and $d_a \approx \frac{4n\lambda}{NA^2}$ respectively,[115] where NA is the numerical aperture, n is the refractive index of the sample, and λ is the wavelength of the laser. The best achievable resolution using Raman spectroscopy with a 100× oil immersion objective (numerical aperture 1.4) is approximately 463 nm for lateral resolution and 1629 nm for axial resolution for a green laser with λ equal to 532 nm.

For example, Poonoosamy *et al.*[54] developed a miniaturized flow-through reactor (Fig. 10a) to study the dissolution of a primary mineral (celestine, $SrSO_4$) followed by the precipitation of a secondary mineral (barite, $BaSO_4$) processes in fractured porous media due to the injection of a reacting solution of barium chloride. By incorporating confocal Raman spectroscopy, these investigations enabled real-time monitoring

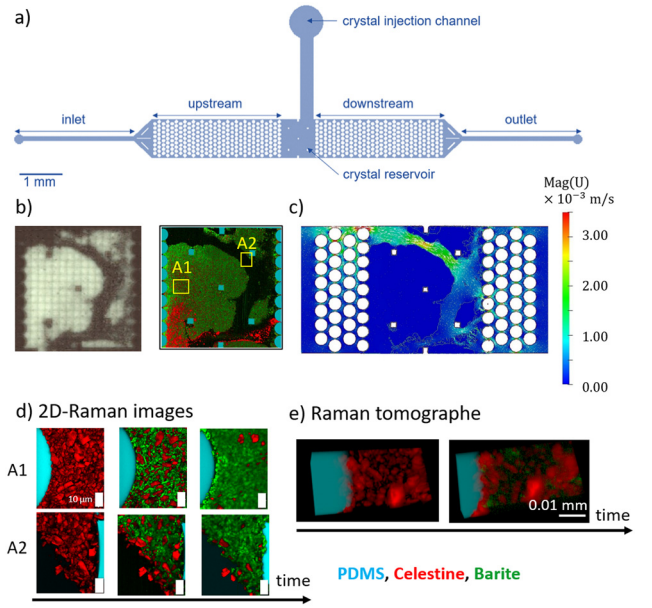

Fig. 10 a) Micronized flow-through microfluidic reactor with a crystal injection channel for injecting micro-sized crystals into the crystal reservoir to form a reactive porous medium. b) Imaging of the reactive fractured porous medium using optical microscopy (left) and Raman spectroscopy (right) after chemical reactions. c) Simulated flow field across the fracture. d) Time-resolved Raman imaging showing the dissolution of the primary mineral celestine (red) and the precipitation of the secondary mineral barite (green). e) 3D Raman imaging of the porous medium before and after the chemical reaction. Reproduced and adapted from Poonoosamy *et al.*[54] with permission from Royal Society of Chemistry, copyright 2020.

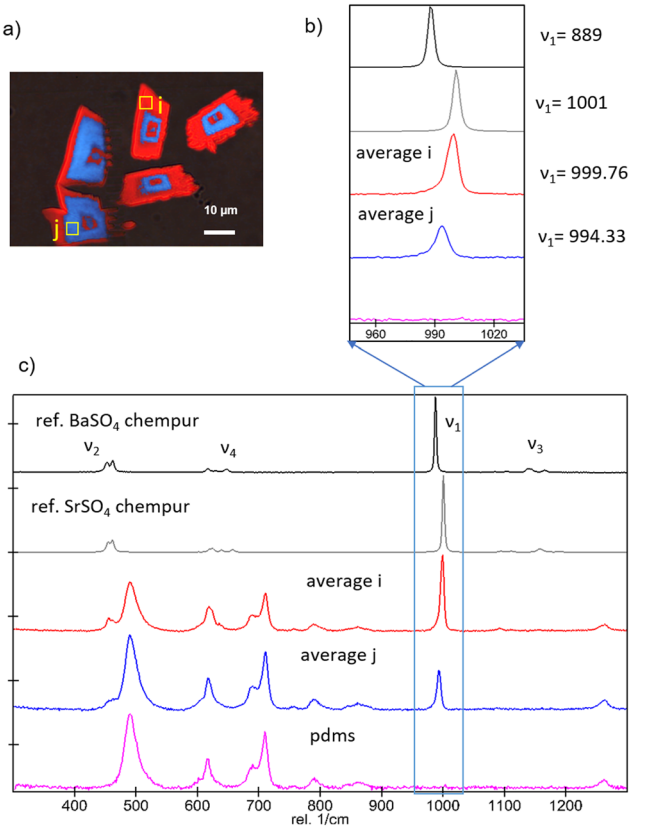

Fig. 11 a) Raman oscillatory zoned crystal of $(Ba_x,Sr_{1-x})SO_4$ with Sr (in red) enriched and Ba (in blue) enriched solid solution. b) and c) Raman signature of reference $BaSO_4$ (barite) and $SrSO_4$ (celestine) and the newly formed phases (i) and (j) with (b) zoom on the prominent sulfate band and (c) the complete spectra. Reproduced from Poonoosamy *et al.*[116] with permission from Springer Nature, copyright 2021.

of the mineralogical transformation at the pore scale, with detailed characterization in both two-dimensional (2D) (Fig. 10b and d) and three-dimensional (3D) (Fig. 10e) geometries. Coupled with pore-scale modeling to map velocity fields (Fig. 10c), this study systematically evaluated the influence of the Péclet number (Pé, the ratio of the advective to diffusive transport) and hydrodynamic heterogeneity on mineral precipitation patterns in porous and fractured systems.[54]

The integration of microfluidic experiments with reactive transport modeling diagnostics also provides a framework for developing mechanistic models to describe contaminant transport and immobilization *via* co-precipitation of solid solutions in porous media. For instance, $BaSO_4$ based solid solutions are known as critical sinks for contaminants like ^{226}Ra, commonly encountered in subsurface energy applications. While thermodynamic models have advanced solubility predictions, they often fall short in capturing the complex dynamics of contaminants in subsurface environments, where co-precipitation is governed by the interplay between solute transport and dissolution-precipitation kinetics, giving rise to phenomena such as oscillatory zoning. Recent studies revisited the oscillatory zoning of $(Ba,Sr)SO_4$ solid solutions using a micronized lab-on-chip device integrating *in situ* micro-Raman spectroscopy.[116]

In Poonoosamy *et al.*,[116] Raman spectra of high-purity $SrSO_4$ and $BaSO_4$ (99.99 from Chempur) and cured PDMS were recorded across the 200–1400 cm^{-1} range, see Fig. 11. Diagnostic vibrational modes of sulfate ions (SO_4^{2-}), including symmetric (ν_1) and anti-symmetric (ν_3) stretching modes, as well as bending modes (ν_2 and ν_4), were used to identify and differentiate phases. The intense $\nu_1(SO_4)$ bands at 988 cm^{-1} for $BaSO_4$ and 1001 cm^{-1} for $SrSO_4$ were well-resolved and free from overlap with PDMS bands. The compositional analysis of $(Ba_x,Sr_{1-x})SO_4$ solid solutions relied on the linear relationship described by Vegard's law that correlates vibrational frequencies with composition. Specifically, the $(\nu_1)(SO_4)$ band maxima positions were interpolated to determine the mole fractions of end-members constituting the solid solution. The accuracy of this approach is inherently dependent on the spectral resolution, as high-resolution spectra are essential for resolving subtle shifts in band positions and capturing stoichiometric variability within the solid solutions. The study demonstrated that oscillatory zoning results from limited solute diffusion and kinetically controlled precipitation, emphasizing the role of nucleation-mediated mineralization in diffusive systems and offering a validated framework to predict solid solution formation and radionuclide mobility under kinetic constraints.

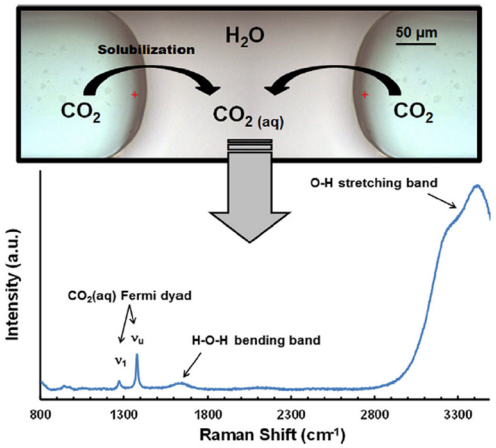

Fig. 12 Optical image of a CO_2–water flow inside a microchannel and corresponding confocal Raman spectra within a water slug containing dissolved CO_2. Reproduced from Liu *et al.*[117] with permission from Elsevier, copyright 2012.

In addition to the identification of solid phases, Raman spectroscopy also enables the identification and quantification of aqueous species in solutions,[117] see Fig. 12. The main advantage here is to avoid the use of fluorescent dyes that may alter the properties of the fluid or the fluid–solid interactions. Active Raman tracers, for example, deuterated water that is chemically inert and has the same properties as water, can be used as tracers and consequently to determine the diffusive properties of newly formed microporous precipitates.[25]

Micro-FTIR spectroscopy to track chemical reactions. The integration of infrared spectroscopy with microfluidics has been successfully demonstrated in several studies.[118,119] Compared to Raman spectroscopy, FTIR offers improved selectivity and quantification capabilities. However, combining FTIR with microfluidic systems remains challenging due to constraints associated with the materials typically used for device fabrication, particularly in terms of transparency and chemical compatibility. Conventional materials such as glass and PDMS exhibit strong absorption in the mid-IR range, which limits their suitability for these applications. Consequently, alternative materials like CaF_2, sapphire, ZnSe, or silicon must be considered for mid-IR transparent microchips. In this context, Barich and Krummel[120] proposed an original approach using conventional PDMS for IR-compatible devices. By exploiting the direct relationship between optical density and material thickness, they designed devices featuring PDMS layers of controlled thicknesses. A thin PDMS film supported on a CaF_2 wafer provided sufficient mid-IR transparency for effective analysis. Overall, FTIR spectroscopy stands out as a powerful, non-invasive technique for real-time chemical analysis in microreactors.[119] Yet, to date, its application in geoscience-related studies, particularly for subsurface processes, remains limited.

Biofilms and bioreactions. The methods presented in this paper apply to the study of biofilms or bioreactions, *e.g.*, Feng *et al.*[121] developed micro-Raman spectroscopy to characterize biofilms.[121] Savorana *et al.*[122] proposed a microfluidic platform dedicated to characterizing the structure and rheology of biofilm streamers. Streamers are biofilm filaments suspended in flow. They cause rapid clogging and affect transport properties. With an epifluorescence microscope Savorana *et al.*[122] characterized the biochemical composition and morphology of the streamers. Moreover, they developed a protocol to perform hydrodynamic stress tests *in situ* to detect differences in the biofilm rheology due to differences in biochemical composition.

Transport through and storage within permeable rocks may depend on the interplay of transport and biochemical reactions. Microbial microorganisms may grow to form biofilms attached to surfaces or that span pores. In turn, biofilms alter fluid flow, thereby influencing further biofilm growth. Kurz *et al.*[123] used porous media micromodels to measure and interpret biofilm growth as a function of pore size and flow rate. Using images and a numerical model, they interpreted the role of biofilms on permeability and the flow field. Additionally, Liu *et al.*[49] used etched-silicon micromodels filled with hydrogen and aqueous solutions containing a halophilic sulfate-reducing bacterium to study the effects of biofilms on hydrogen loss, rock wettability, and porous medium transport processes. The consumption rate of hydrogen was affected significantly by the gas-water interfacial area and the activity of the microbes. These studies teach that porous media clogged with biofilms do not behave similar to expectations derived from heterogeneity and abiotic reaction products in porous media. Generally, microfluidics is underutilized despite the clear benefits of visualizing biofilms and the progression of bioreactions directly.

Current limitations in tracking chemical reactions. Using tracers seeded in fluids to measure concentration fields, pH, or monitor reactive fronts introduces the drawback of adding an additional chemical component to the system. These tracers may alter the fluid properties, interact with the solution or channel materials, degrade over time, produce overlapping signals with other species, or be chemically incompatible with the reaction of interest. As an alternative, spectroscopic methods offer the advantage of non-invasive analysis, avoiding the need to introduce external species. As will be discussed in the Future challenges section, however, tracking dissolved species using spectroscopic techniques is not always straightforward.

3.4 Computational microfluidics

Microfluidics experiments are useful to inform and complement numerical simulations. High-fidelity measurements obtained during micromodel experiments are used to verify the predictions by numerical models at the pore scale. These computational microfluidics[45] are augmented depending on the comparison with experimental data. Microfluidic experiments generate valuable benchmark datasets that enhance the accuracy and reliability of numerical solvers.[20,44,100,124] Conversely, numerical simulations complement microfluidic experiments by offering high-resolution insights into pressure

and velocity profiles, solute concentration, and mineral distribution—parameters that are challenging to measure experimentally. For example, the flow field within a microfluidic device can be calculated numerically to help interpret mineral reactivity[54] or clay deposition in the devices.[57] Sugar *et al.*[125] combined microfluidics and numerical simulations to assess the retention mechanisms of polymers arising during flow and their impact on apparent permeability. Ollivier-Triquet *et al.*[126] used the lattice Boltzmann method to calculate velocity and concentration fields for experimental microfluidic images and show that unsaturated porous media exhibit anomalous dispersion. Hassannayebi *et al.*[127] used a digital-twin approach, *i.e.*, segmented microfluidic experimental images of biomass accumulation are used to perform Navier–Stokes–Brinkmann flow simulations. They consider the accumulated biomass as permeable or impermeable in the model based on the optical density of the biomass in the images. The comparison between simulation results and experimental responses shows that biomass accumulation in porous media is a permeable medium.[127] In conclusion, the combined application of experimental and computational microfluidics offers a robust method for unraveling the complex mechanisms occurring in soils and the subsurface.

3.5 From microfluidics to field-scale

One limitation of micromodels is that they are two-dimensional. To consider multiscale pore sizes, dual-porosity, and dual-depth micromodels have been developed.[38,80,128] Nevertheless, extrapolation of results to three-dimensional systems must be done carefully. Microfluidic devices will never represent the 3D connectivity of the pores of a rock sample. Some authors attempted to reproduce 3D core flood experiments on microfluidic devices,[39] however, these devices do not have the features of 3D core floods. The purpose of micromodel experiments in geosciences is not to achieve a direct, one-to-one comparison with real rock samples. Instead, they serve to isolate specific mechanisms and examine chemical changes within simplified porous media. The following methods can then be used to extrapolate these findings to larger-scale systems.

Core flooding experiments. Core-flooding experiments allow the use of real rock samples, thus preserving the natural mineral heterogeneity, pore structure, and wettability. Even using synthetic materials, the pore connectivity, porosity, and permeability are representative of reservoir conditions. Despite major advances in 3D imaging, while being resolved in time and space,[129] microfluidics offers better control over the heterogeneity and the geometry for fundamental studies of the processes. Nevertheless, microfluidics and core-flood experiments are complementary.[130] Core-flood data are usable for reservoir modeling, while microfluidics provide details on interfacial phenomena, and high-resolution visualization of the pore-scale mechanisms that help interpret core-scale data.[46]

Numerical upscaling. Numerical upscaling refers to the use of experimental data (physicochemical parameters, geometry, processes, transport laws, and so on) to provide macroscale data or models. Integrating data from experiments, numerical experiments can be carried out for various pore structures representative of natural pore networks, including 3D images of rocks,[131–134] This numerical upscaling informs large-scale properties, *e.g.*, mean dissolution rate, dispersion tensor, interfacial area, saturation, solubility, flow rate, and characteristic pore size. Effective properties can also be obtained from experiments and used as input for macroscale models.[135]

Integrating Raman tomography within microfluidic chips, combined with pore-scale modeling, offers a robust approach to determine the transport properties of chemically evolving porous media and to evaluate constitutive equations, such as the relationship between porosity and diffusivity, as demonstrated by Poonoosamy *et al.* (2022).[24]

Geoelectrical monitoring on a chip. Geophysical methods are used to image and characterize processes in geological environments.[136] They measure spatial and temporal variations in the physical properties of the subsurface using measuring devices and sensors. However, identifying the electrical signatures that are unique for each process involved is challenging. So far, studies have combined laboratory experiments with petrophysical models to interpret geoelectrical signals. Interpreting macroscopic geoelectrical data can sometimes be ambiguous, as it relies on microscopic parameterization that the traditional experimental column approach can only infer. Rembert *et al.*[137] developed the first microfluidic chips equipped with electrodes for geoelectrical monitoring using the spectral induced polarization (SIP) method. Equipping microfluidic devices for geoelectrical acquisition brings a new understanding of these indirect physical measurements in the light of explicit descriptions of flows, reactions, and transport mechanisms, thus bridging the gap between pore-scale events and field-scale interpretations. The proposed technological advancement paves the way for further understanding of the subsurface processes through geoelectrical observation.[138] Future challenges are to introduce spatial discretization using arrays of electrodes within microfluidic devices. In addition, the setup could be adapted to use the self-potential method, a passive technique to map the electrical potential distribution generated by fluid flow and chemical reactions.[139,140]

4 Future challenges

In this section, we discuss some of the future challenges in measurement capacity during micromodel experiments for geosciences applications.

Towards characterization of minerals on a chip

In recent years, the integration of microfluidic platforms with advanced microstructural analysis techniques has significantly advanced the study of chemical and structural alterations in porous media. Notably, the incorporation of Raman spectroscopy directly onto microfluidic chips has

enabled *in situ* investigations of chemical changes at high spatial and temporal resolution.

Microfluidics coupled with Raman can be further enhanced to study slower or more complex processes through the use of isotopic tracers, such as ^{18}O, commonly employed in batch experiments[141] to monitor coupled mineral dissolution and carbonate precipitation. It was used to unlock key processes for CO_2 sequestration in basaltic rocks.

Future advancements may involve the use of in-operando synchrotron-based techniques,[17,142,143] such as micro-XRD or micro-XRF[144] (μ-XRD and μ-XRF), to provide unprecedented spatial resolution of mineral distribution structures during reactive processes. The use of X-ray laminography to monitor the evolution of a 3D reactive porous medium on a chip has been demonstrated by Morais *et al.*[145] Additionally, modern microfluidics now allows the retrieval of alteration products upon opening, for advanced electron microscopy analyses, such as focused ion beam scanning electron microscopy (FIB-SEM)[59] or scanning transmission electron microscopy (STEM), to probe micro- and nano-porosity in newly formed precipitates. Techniques such as atomic force microscopy (AFM) can further elucidate surface-level processes, offering detailed insights into mineral growth and dissolution dynamics. These combined approaches open new avenues for understanding geochemical processes at multiple scales.

Tracking solutes

Measuring concentrations or distributions of species in solution can be essential.[43] The use of dyes to track dissolved species presents some limitations, in particular, it can modify the properties of the fluid (density, viscosity, fluid–fluid, or fluid–solid properties). Moreover, three-dimensional measurement of concentration fields is still challenging.[112] Quantification of aqueous solutions using Raman spectroscopy is feasible; however, careful optimization of laser power, measurement duration, and, particularly in microfluidic systems, the reactor's depth is essential to minimize interference from the reactor's intrinsic spectral signature that could compromise the accuracy of quantitative analysis.[117] Thus, future developments should be considered to determine the relationship between solute concentration and Raman band intensity for various dissolved species, *e.g.*, salts, dissolved inorganic carbon, organic compounds, and/or chlorinated compounds.

Measure local pressure fields

Pressure measurements are of crucial importance to describe and understand flow properties, in particular for studies of two-phase flow in porous media. So far, pressure measurements are commonly performed at the inlet and outlet of microfluidic devices using pressure sensors, thus without information on the pore-scale distribution of pressures. Several miniature pressure sensors,[146,147] or *in situ* pressure measurement methods have been proposed Abkarian *et al.*,[148] Shen *et al.*[149] The characterization of pressures for various micromodel designs has been greatly improved in recent years,[150] however, mapping pressure distribution in complex porous media geometries is still challenging.

Towards an AI-assistance for microfluidic experiments

Combining microfluidic experiments with pore-scale modeling presents considerable challenges, including high computational demands that often require high-performance computing environments and time-intensive data processing, particularly for image segmentation. As a result, datasets produced through these resource-intensive workflows are frequently underutilized. To harness fully the potential of high-throughput experiments, it is essential to implement automated evaluation processes and eliminate bottlenecks that hinder analysis. Machine learning provides a promising solution to address these limitations at various stages of the workflow. For instance, in biotechnology, automated monitoring systems and live segmentation techniques are commonly used to study cellular and bacterial growth.[151,152] Similarly, in porous media research, convolutional neural network (CNN) models have been successfully applied to estimate parameters such as effective diffusivity,[153] permeability, wettability,[154] and aqueous-fluid chemistry[155] with significantly lower computational costs compared to traditional simulations. Creating a toolkit for experimentalists that supports (i) image segmentation and pattern recognition and (ii) predictive modeling of aqueous solution chemistry on the fly could have a huge potential as an analytical tool in the field. Such a framework would enable real-time analysis of physical and chemical processes, allowing researchers to dynamically adjust experimental conditions and providing the flexibility to explore specific processes by modifying boundary conditions at various stages of their experiment.

Conclusions

Natural porous media are captivating systems where the intricate interplay of physicochemical processes across multiple scales govern the dynamics of subsurface environments. Achieving a comprehensive understanding of transport processes in geological formations is essential for advancing the sustainable management of natural resources, including geothermal energy, hydrocarbons, gas storage, nuclear waste disposal, and groundwater. These transport phenomena involve complex multifluid and multiscale flow challenges, where microscale interactions propagate to influence macroscopic behavior.

Microfluidics has emerged as an indispensable tool for investigating the coupled processes occurring at the pore scale in subsurface environments. By providing high-resolution spatiotemporal datasets, microfluidic experiments complement traditional column-scale laboratory studies and numerical simulations. These experiments enable precise measurements of velocity fields, fluid–fluid interfaces, solute

concentrations, and mineral distributions, facilitating a deeper understanding of the fundamental physicochemical mechanisms at play. Moreover, the data generated from microfluidic experiments serve as critical benchmarks for numerical models, enhancing their predictive capabilities and improving the fidelity of large-scale geological models.

This review outlined recent advances in microfluidic methodologies tailored for geosciences, with a focus on measuring fluid distributions, velocity and concentration fields, and tracking chemical reactions. The integration of microfluidic experiments with computational microfluidics offers unparalleled insights into pore-scale hydrogeochemical properties, significantly advancing our understanding of subsurface processes.

Despite these achievements, challenges remain in further refinement of measurement capabilities, scaling experimental results to field-relevant conditions, and addressing the inherent complexities of natural systems. Future research must aim to bridge these gaps, enabling even more precise characterization of subsurface processes. The synergistic use of experimental and computational microfluidics paves the way for improved physical understanding, more robust models, and sustainable management strategies for Earth's critical subsurface resources.

Data availability

No primary research results, software or code have been included, and no new data were generated or analysed as part of this review.

Author contributions

Conceptualization, S. R.; writing – original draft, S. R. and J. P.; writing – review & editing, S. R., F. R., A. R. K., and J. P.; funding acquisition, S. R., and J. P.

Conflicts of interest

There are no conflicts to declare.

Acknowledgements

S. R. thanks the European Union (ERC, TRACE-it, grant agreement no. 101039854), and the French National Research Agency (ANR) (grant number ANR-21-CE50-0038) for funding research related to microfluidics for geosciences. J. P. thank the European Union GENIES (ERC, GENIES grant agreement no. 101040341) for funding research related to microfluidics and subsurface energy-related applications.

Notes and references

1 G. Whitesides, *Nature*, 2006, **442**, 368–373.
2 C. Mattax and J. Kyte, *Oil Gas J.*, 1961, **59**, 115–128.
3 A. Manz, N. Graber and H. Widmer, *Sens. Actuators, B*, 1990, **1**, 244–248.
4 E. Ruiz-Agudo, C. Putnis and A. Putnis, *Chem. Geol.*, 2014, **383**, 132–146.
5 C. Noiriel, L. Luquot, B. Madé, L. Raimbault, P. Gouze and J. van der Lee, *Chem. Geol.*, 2009, **265**, 160–170.
6 S. S. Datta, I. Battiato, M. A. Fernø, R. Juanes, S. Parsa, V. Prigiobbe, E. Santanach-Carreras, W. Song, S. L. Biswal and D. Sinton, *Lab Chip*, 2023, **23**(5), 1358–1375.
7 T. Zhang, G. V. Lowry, N. L. Capiro, J. Chen, W. Chen, Y. Chen, D. D. Dionysiou, D. W. Elliott, S. Ghoshal, T. Hofmann, H. Hsu-Kim, J. Hughes, C. Jiang, G. Jiang, C. Jing, M. Kavanaugh, Q. Li, S. Liu, J. Ma, B. Pan, T. Phenrat, X. Qu, X. Quan, N. Saleh, P. J. Vikesland, Q. Wang, P. Westerhoff, M. S. Wong, T. Xia, B. Xing, B. Yan, L. Zhang, D. Zhou and P. J. J. Alvarez, *Environ. Sci.: Nano*, 2019, **6**, 1283–1302.
8 S. Kumar, J. Foroozesh, K. Edlmann, M. G. Rezk and C. Y. Lim, *J. Nat. Gas Sci. Eng.*, 2020, **81**, 103437.
9 B. Agaoglu, N. K. Copty, T. Scheytt and R. Hinkelmann, *Adv. Water Resour.*, 2015, **79**, 162–194.
10 S. Roman, C. Soulaine and A. R. Kovscek, *J. Colloid Interface Sci.*, 2020, **558**, 269–279.
11 M. Lysyy, G. Ersland and M. Fernø, *Adv. Water Resour.*, 2022, **163**, 104167.
12 W. van Rooijen, L. Hashemi, M. Boon, R. Farajzadeh and H. Hajibeygi, *Adv. Water Resour.*, 2022, **164**, 104221.
13 M. Riazi, M. Sohrabi, C. Bernstone, M. Jamiolahmady and S. Ireland, *Chem. Eng. Res. Des.*, 2011, **89**, 1827–1840.
14 C. Zhang, M. Oostrom, J. W. Grate, T. W. Wietsma and M. G. Warner, *Environ. Sci. Technol.*, 2011, **45**, 7581–7588.
15 S. Roman, C. Soulaine, M. AbuAlSaud, A. Kovscek and H. Tchelepi, *Adv. Water Resour.*, 2016, **95**, 199–211.
16 S. Morais, N. Liu, A. Diouf, D. Bernard, C. Lecoutre, Y. Garrabos and S. Marre, *Lab Chip*, 2016, **16**, 3493–3502.
17 Y. Li, F. Kazemifar, G. Blois and K. T. Christensen, *Water Resour. Res.*, 2017, **53**(7), 6178–6196.
18 C. Chang, Q. Zhou, M. Oostrom, T. J. Kneafsey and H. Mehta, *Adv. Water Resour.*, 2017, **100**, 14–25.
19 R. Singh, M. Sivaguru, G. A. Fried, B. W. Fouke, R. A. Sanford, M. Carrera and C. J. Werth, *J. Contam. Hydrol.*, 2017, **204**, 28–39.
20 C. Soulaine, S. Roman, A. R. Kovscek and H. A. Tchelepi, *J. Fluid Mech.*, 2017, **827**, 457–483.
21 W. Song, F. Ogunbanwo, M. Steinsbø, M. A. Fernø and A. R. Kovscek, *Lab Chip*, 2018, **18**(5), 3881–3891.
22 J. Poonoosamy, C. Westerwalbesloh, G. Deissmann, M. Mahrous, E. Curti, S. V. Churakov, M. Klinkenberg, D. Kohlheyer, E. von Lieres, D. Bosbach and N. I. Prasianakis, *Chem. Geol.*, 2019, **528**, 119264.
23 H. Yoon, K. N. Chojnicki and M. J. Martinez, *Environ. Sci. Technol.*, 2019, **53**, 14233–14242.
24 J. Poonoosamy, R. Lu, M. I. Lönartz, G. Deissmann, D. Bosbach and Y. Yang, *Energies*, 2022, **15**, 2160.
25 M. Lönartz, Y. Yang, G. Deissmann, D. Bosbach and J. Poonoosamy, *Water Resour. Res.*, 2023, **59**(11), e2023WR034722.
26 C. Zhao, Y. Xiao, J. Chu, R. Hu, H. Liu, X. He, Y. Liu and X. Jiang, *Acta Geotech.*, 2023, **18**, 5299–5318.

27 J. Poonoosamy, A. Obaied, G. Deissmann, N. I. Prasianakis, M. Kindelmann, B. Wollenhaupt, D. Bosbach and E. Curti, *Commun. Chem.*, 2023, **6**, 250.
28 J. Poonoosamy, A. Kaspor, C. Schreinemachers, D. Bosbach, O. Cheong, P. Kowalski and A. Obaied, *Sci. Rep.*, 2024, **14**(1), 9502.
29 S. Morais, A. Cario, N. Liu, D. Bernard, C. Lecoutre, Y. Garrabos, A. Ranchou-Peyruse, S. Dupraz, M. Azaroual, R. Hartman and S. Marre, *React. Chem. Eng.*, 2020, **5**(7), 1156–1185.
30 Y. Zhong, Q. Li, W. Gao, Y. Wen and Y. Zhang, *J. Rock Mech. Geotech. Eng.*, 2025, DOI: **10.1016/j.jrmge.2025.01.018**.
31 A. Ratanpara, Y. Li and M. Kim, *Lab Chip*, 2025, Advance Article.
32 V. A. Lifton, *Lab Chip*, 2016, **16**, 1777–1796.
33 N. K. Karadimitriou and S. M. Hassanizadeh, *Vadose Zone J.*, 2012, vzj2011.0072.
34 A. Anbari, H.-T. Chien, S. S. Datta, W. Deng, D. A. Weitz and J. Fan, *Small*, 2018, **14**, 1703575.
35 A. Jahanbakhsh, K. L. Wlodarczyk, D. P. Hand, R. R. J. Maier and M. M. Maroto-Valer, *Sensors*, 2020, **20**, 4030.
36 L. Cha, C. Xie, Q. Feng and M. Balhoff, *Water Resour. Res.*, 2021, **57**, e2020WR029476.
37 M. Buchgraber, M. Al-Dossary, C. Ross and A. Kovscek, *J. Pet. Sci. Eng.*, 2012, **86-87**, 27–38.
38 W. Yun, C. M. Ross, S. Roman and A. R. Kovscek, *Lab Chip*, 2017, **17**, 1462–1474.
39 L. Mejia, P. Zhu, J. D. Hyman, K. K. Mohanty and M. T. Balhoff, *Fuel*, 2020, **281**, 118716.
40 W. Song, T. W. de Haas, H. Fadaei and D. Sinton, *Lab Chip*, 2014, **14**, 4382–4390.
41 M. Porter, J. Jimenez-Martinez, R. Martinez, Q. McCulloch, B. Carey and H. Viswanathan, *Lab Chip*, 2015, **15**, 4044–4053.
42 F. Osselin, P. Kondratiuk, A. Budek, O. Cybulski, P. Garstecki and P. Szymczak, *Geophys. Res. Lett.*, 2016, **43**, 6907–6915.
43 Y. M. Corapcioglu, S. Chowdhury and S. E. Roosevelt, *Water Resour. Res.*, 1997, **33**, 2547–2558.
44 C. Soulaine, S. Roman, A. R. Kovscek and H. A. Tchelepi, *J. Fluid Mech.*, 2018, **855**, 616–645.
45 C. Soulaine, J. Maes and S. Roman, *Front. Water*, 2021, **3**, 11.
46 T. Sun, J. Song, Z. Liu and W. Jiang, *J. Environ. Sci.*, 2022, **113**, 365–375.
47 N. Delouche, A. B. Schofield and H. Tabuteau, *Soft Matter*, 2020, **16**, 9899–9907.
48 S. H. Lee, E. Secchi and P. K. Kang, *Proc. Natl. Acad. Sci. U. S. A.*, 2023, **120**, e2204466120.
49 N. Liu, A. R. Kovscek, M. A. Fernø and N. Dopffel, *Front. Energy Res.*, 2023, **11**, 1124621.
50 S. Roman, M. O. Abu-Al-Saud, T. Tokunaga, J. Wan, A. R. Kovscek and H. A. Tchelepi, *J. Colloid Interface Sci.*, 2017, **507**, 279–289.
51 L. He, Z. Luo and B. Bai, *Chem. Eng. Sci.*, 2020, **220**, 115649.
52 N. Nazari, W. Yun and A. R. Kovscek, *J. Colloid Interface Sci.*, 2023, **638**, 149–160.
53 J. Hornbrook, L. Castanier and P. Pettit, *SPE Annual Technical Conference and Exhibition*, Dallas, Texas, 1991, SPE-22631-MS.
54 J. Poonoosamy, C. Soulaine, A. Burmeister, G. Deissmann, D. Bosbach and S. Roman, *Lab Chip*, 2020, **20**, 2562–2571.
55 J. Xu and M. T. Balhoff, *Lab Chip*, 2022, **22**, 4205–4223.
56 J. Xu and M. T. Balhoff, *Adv. Water Resour.*, 2022, **164**, 104200.
57 W. Song and A. Kovscek, *Lab Chip*, 2015, **15**, 3314–3325.
58 Y. Zhang, G. Yesiloz, H. J. Sharahi, H. Khorshidian, S. Kim, A. Sanati-Nezhad and S. H. Hejazi, *Adv. Mater. Interfaces*, 2019, 1900995.
59 B. Ling, M. Sodwatana, A. Kohli, C. M. Ross, A. Jew, A. R. Kovscek and I. Battiato, *Proc. Natl. Acad. Sci. U. S. A.*, 2022, **119**, e2122520119.
60 J. Jiménez-Martínez, J. D. Hyman, Y. Chen, J. W. Carey, M. L. Porter, Q. Kang, G. Guthrie Jr and H. S. Viswanathan, *Geophys. Res. Lett.*, 2020, **47**, e2020GL087163.
61 D. George, O. Hayat and A. Kovscek, *J. Pet. Sci. Eng.*, 2005, **46**, 101–119.
62 B. Benali, T. L. Føyen, Z. P. Alcorn, M. Haugen, J. Gauteplass, A. R. Kovscek and M. A. Fernø, *Int. J. Greenhouse Gas Control*, 2022, **114**, 103607.
63 M. Lysyy, N. Liu, D. Landa-Marbán, G. Ersland and M. Fernø, *J. Energy Storage*, 2024, **87**, 111439.
64 J. McDonald, D. Duffy, J. Anderson, D. Chiu, H. Wu, O. Schueller and G. Whitesides, *Electrophoresis*, 2000, **21**, 27–40.
65 A. P. Dimou, H. P. Menke and J. Maes, *Transp. Porous Media*, 2022, **141**, 279–294.
66 A. Gerami, Y. Alzahid, P. Mostaghimi, N. Kashaninejad, F. Kazemifar, T. Amirian, N. Mosavat, M. E. Warkiani and R. T. Armstrong, *Transp. Porous Media*, 2018, **130**, 277–304.
67 S. Marre, A. Adamo, S. Basak, C. Aymonier and K. F. Jensen, *Ind. Eng. Chem. Res.*, 2010, **49**, 11310–11320.
68 S. Morais, E. Vidal, A. Cario, S. Marre and A. Ranchou-Peyruse, *FEMS Microbiol. Ecol.*, 2024, **100**, fiae151.
69 M. Buchgraber, A. R. Kovscek and L. M. Castanier, *Transp. Porous Media*, 2012, **95**, 647–668.
70 S. Marre, C. Lecoutre, Y. Garrabos, C. Fauveau, A. Cario and O. Nguyen, Sapphire Microreactors, *EP*, 21722965.7, 2024.
71 V. Gredicak, C. Douat, A. Slodczyk, S. Dozias and S. Roman, *Microfluid. Nanofluid.*, 2025, **29**, 22.
72 Q. Zhang, N. Karadimitriou, S. Hassanizadeh, P. Kleingeld and A. Imhof, *J. Colloid Interface Sci.*, 2013, **401**, 141–147.
73 N. K. Karadimitriou, M. Musterd, P. J. Kleingeld, M. T. Kreutzer, S. M. Hassanizadeh and V. Joekar-Niasar, *Water Resour. Res.*, 2013, **49**, 2056–2067.
74 T. Trantidou, Y. Elani, E. Parsons and O. Ces, *Microsyst. Nanoeng.*, 2017, **3**, 1–9.
75 S. Tan, N. Nguyen, Y. Chua and T. Kang, *Biomicrofluidics*, 2010, **4**, 032204.
76 B. Zhao, C. W. MacMinn and R. Juanes, *Proc. Natl. Acad. Sci. U. S. A.*, 2016, **113**, 10251–10256.
77 A. M. Saad, M. P. Yutkin, C. J. Radke and T. W. Patzek, *Energy Fuels*, 2022, **36**, 5647–5656.
78 A. R. Kovscek, H. Wong and C. J. Radke, *AIChE J.*, 1993, **39**, 1072–1085.
79 S. Aldousary and A. R. Kovscek, *J. Pet. Sci. Eng.*, 2019, **179**, 606–614.

80 C. Chang, T. J. Kneafsey, J. Wan, T. K. Tokunaga and S. Nakagawa, *Water Resour. Res.*, 2020, e2019WR026789.
81 A. AlOmier, D. Cha, S. Ayirala, A. Al-Yousef and H. Hoteit, *Lab Chip*, 2024, **24**, 882–895.
82 C. Brigodiot, E. Speirs, C. Guyon, M. Tatoulian and N. Pannacci, *Soft Matter*, 2025, **21**, 2509–2517.
83 J. Lim, *Two-dimensional Signal and Image Processing*, 1990.
84 C. Chang, Q. Zhou, T. J. Kneafsey, M. Oostrom, T. W. Wietsma and Q. Yu, *Adv. Water Resour.*, 2016, **92**, 142–158.
85 C. Zhang, M. Oostrom, T. W. Wietsma, J. W. Grate and M. G. Warner, *Energy Fuels*, 2011, **25**, 3493–3505.
86 R. Lenormand, E. Touboul and C. Zarcone, *J. Fluid Mech.*, 1988, **189**, 165–187.
87 C. J. Werth, C. Zhang, M. L. Brusseau, M. Oostrom and T. Baumann, *J. Contam. Hydrol.*, 2010, **113**, 1–24.
88 N. K. Karadimitriou, S. M. Hassanizadeh, V. Joekar-Niasar and P. J. Kleingeld, *Water Resour. Res.*, 2014, **50**, 8125–8140.
89 S. Roman, A. Merlo, P. Duru, F. Risso and S. Lorthois, *Biomicrofluidics*, 2016, **10**, 034103.
90 O. Borgman, R. Turuban, B. Géraud, T. Le Borgne and Y. Méheust, *Geophys. Res. Lett.*, 2023, **50**, e2022GL101407.
91 F. P. Bretherton, *J. Fluid Mech.*, 1961, **10**, 166–188.
92 L. M. Peurrung, M. Rashidi and T. J. Kulp, *Chem. Eng. Sci.*, 1995, **50**, 2243–2253.
93 J. Santiago, S. Wereley, C. Meinhart, D. Beebe and R. Adrian, *Exp. Fluids*, 1998, **25**, 316–319.
94 R. Lindken, S. Rossi, M. Große and J. Westerweel, *Lab Chip*, 2009, **9**, 2551–2567.
95 W. Thielicke and E. Stamhuis, *J. Open Res. Softw.*, 2014, **2**, 30.
96 G. Blois, J. Barros and K. Christensen, *Microfluid. Nanofluid.*, 2015, 1–16.
97 M. Heshmati and M. Piri, *Fuel*, 2018, **224**, 560–578.
98 R. Adrian and J. Westerweel, *Particle Image Velocimetry*, Cambridge University Press, 2011.
99 J. S. Park, C. K. Choi and K. D. Kihm, *Exp. Fluids*, 2004, **37**, 105–119.
100 D. Sen, D. S. Nobes and S. K. Mitra, *Microfluid. Nanofluid.*, 2012, **12**, 189–200.
101 T. T. Truscott, J. Belden, R. Ni, J. Pendlebury and B. McEwen, *Exp. Fluids*, 2017, **58**, 16.
102 X. Song, J. Li, M. Gu and C. Xu, *Opt. Commun.*, 2020, **475**, 126302.
103 F. Kazemifar, G. Blois, D. C. Kyritsis and K. T. Christensen, *Adv. Water Resour.*, 2016, **95**, 352–368.
104 N. Seigneur, K. U. Mayer and C. I. Steefel, *Rev. Mineral. Geochem.*, 2019, **85**, 197–238.
105 A. Heinrichs, *Nat. Cell Biol.*, 2009, **11**, S7–S7.
106 M. M. Salek, F. Carrara, J. Zhou, R. Stocker and J. Jimenez-Martinez, *Adv. Sci.*, 2024, 2310121.
107 M. Kim, A. Sell and D. Sinton, *Lab Chip*, 2013, **13**, 2508–2518.
108 C. Steefel, *Reactive transport modeling: Applications in subsurface energy and environmental problems*, John Wiley & Sons, 2018.
109 L. Florea, C. Fay, E. Lahiff, T. Phelan, N. E. O'Connor, B. Corcoran, D. Diamond and F. Benito-Lopez, *Lab Chip*, 2013, **13**, 1079–1085.
110 X. Zhang, Z. Dou, M. Hamada, P. de Anna and J. Jimenez-Martinez, *Environ. Sci. Technol.*, 2024, **59**(2), 1334–1343.
111 P. de Anna, J. Jimenez-Martinez, H. Tabuteau, R. Turuban, T. Le Borgne, M. Derrien and Y. Méheust, *Environ. Sci. Technol.*, 2014, **48**, 508–516.
112 S. Izumoto, J. Heyman, J. A. Huisman, K. De Vriendt, C. Soulaine, F. Gomez, H. Tabuteau, Y. Méheust and T. Le Borgne, *Water Resour. Res.*, 2023, **59**, e2023WR034749.
113 A. F. Chrimes, K. Khoshmanesh, P. R. Stoddart, A. Mitchell and K. Kalantar-zadeh, *Chem. Soc. Rev.*, 2013, **42**, 5880–5906.
114 V. Boyd, H. Yoon, C. Zhang, M. Oostrom, N. Hess, B. Fouke, A. J. Valocchi and C. J. Werth, *Geochim. Cosmochim. Acta*, 2014, **135**, 321–335.
115 N. J. Everall, *Analyst*, 2010, **135**, 2512–2522.
116 J. Poonoosamy, M. Mahrous, E. Curti, D. Bosbach, G. Deissmann, S. V. Churakov, T. Geisler and N. Prasianakis, *Sci. Rep.*, 2021, **11**, 23678.
117 N. Liu, C. Aymonier, C. Lecoutre, Y. Garrabos and S. Marre, *Chem. Phys. Lett.*, 2012, **551**, 139–143.
118 K. L. A. Chan, X. Niu, A. J. de Mello and S. G. Kazarian, *Lab Chip*, 2010, **10**, 2170–2174.
119 A. Perro, G. Lebourdon, S. Henry, S. Lecomte, L. Servant and S. Marre, *React. Chem. Eng.*, 2016, **1**, 577–594.
120 M. V. Barich and A. T. Krummel, *Anal. Chem.*, 2013, **85**, 10000–10003.
121 J. Feng, C. De La Fuente-Núñez, M. J. Trimble, J. Xu, R. E. Hancock and X. Lu, *Chem. Commun.*, 2015, **51**, 8966–8969.
122 G. Savorana, J. Słomka, R. Stocker, R. Rusconi and E. Secchi, *Soft Matter*, 2022, **18**, 3878–3890.
123 D. L. Kurz, E. Secchi, R. Stocker and J. Jimenez-Martinez, *Environ. Sci. Technol.*, 2023, **57**, 5666–5677.
124 S. Molins, C. Soulaine, N. I. Prasianakis, A. Abbasi, P. Poncet, A. J. Ladd, V. Starchenko, S. Roman, D. Trebotich and H. A. Tchelepi, *et al.*, *Comput. Geosci.*, 2020, 1–34.
125 A. Sugar, M. Serag, U. Buttner, M. Fahs, S. Habuchi and H. Hoteit, *Sci. Rep.*, 2023, **13**(1), 8245.
126 E. Ollivier-Triquet, B. Braconnier, V. Gervais-Couplet, S. Youssef, L. Talon and D. Bauer, *Adv. Water Resour.*, 2024, **191**, 104774.
127 N. Hassannayebi, B. Jammernegg, J. Schritter, P. Arnold, F. Enzmann, M. Kersten, A. P. Loibner, M. Fernø and H. Ott, *Transp. Porous Media*, 2021, **139**, 579–593.
128 C.-W. Tsao, Q.-Z. Huang, C.-Y. You, M. Hilpert, S.-Y. Hsu, K. Lamorski, L.-C. Chang and C. Sławiński, *Lab Chip*, 2021, **21**, 385–396.
129 T. Bultreys, S. Ellman, C. M. Schlepütz, M. N. Boone, G. K. Pakkaner, S. Wang, M. Borji, S. Van Offenwert, N. Moazami Goudarzi, W. Goethals, C. W. Winardhi and V. Cnudde, *Proc. Natl. Acad. Sci. U. S. A.*, 2024, **121**, e2316723121.
130 M. Tahir, R. E. Hincapie, N. Langanke and L. Ganzer, *SPE Europec featured at EAGE Conference and Exhibition*, SPE Europec, 2020, p. D021S012R002.
131 A. Raeini, B. Bijeljic and M. Blunt, *Transp. Porous Media*, 2014, **101**, 191–213.
132 M. J. Blunt, B. Bijeljic, H. Dong, O. Gharbi, S. Iglauer, P. Mostaghimi, A. Paluszny and C. Pentland, *Adv. Water Resour.*, 2013, **51**, 197–216.

133 C. Soulaine, F. Gjetvaj, C. Garing, S. Roman, A. Russian, P. Gouze and H. A. Tchelepi, *Transp. Porous Media*, 2016, 1–17.
134 M. Prodanović, M. Esteva, J. Mcclure, B. Chang, J. E. Santos, A. Radhakrishnan, A. Singh and H. Khan, *E3S Web Conf.*, 2023, **367**, 01010.
135 T. Bahar, F. Golfier, C. Oltéan, E. Lefevre and C. Lorgeoux, *J. Contam. Hydrol.*, 2018, **211**, 49–64.
136 T. Hermans, P. Goderniaux, D. Jougnot, J. H. Fleckenstein, P. Brunner, F. Nguyen, N. Linde, J. A. Huisman, O. Bour, J. L. Alvis, R. Hoffmann, A. Palacios, A.-K. Cooke, A. Pardo-Álvarez, L. Blazevic, B. Pouladi, P. Haruzi, A. Fernandez Visentini, G. E. H. Nogueira, J. Tirado-Conde, M. C. Looms, M. Kenshilikova, P. Davy and T. Le Borgne, *Hydrol. Earth Syst. Sci.*, 2023, **27**, 255–287.
137 F. Rembert, A. Stolz, C. Soulaine and S. Roman, *Lab Chip*, 2023, **23**, 3433–3442.
138 F. Rembert, P. Leroy, A. Lassin and S. Roman, *Geophys. Res. Lett.*, 2024, **51**, e2024GL111271.
139 L. Jouniaux, A. Maineult, V. Naudet, M. Pessel and P. Sailhac, *C. R. Geosci.*, 2009, **341**, 928–936.
140 F. Rembert, N. M. Fernandez, L. Luquot, R. Guérin and D. Jougnot, *Adv. Water Resour.*, 2025, 104879.
141 T. Geisler, C. Perdikouri, A. Kasioptas and M. Dietzel, *Geochim. Cosmochim. Acta*, 2012, **90**, 1–11.
142 H. Deng, J. P. Fitts, R. V. Tappero, J. J. Kim and C. A. Peters, *Environ. Sci. Technol.*, 2020, **54**, 12502–12510.
143 D. Radajewski, L. Hunter, X. He, O. Nahi, J. M. Galloway and F. C. Meldrum, *Lab Chip*, 2021, **21**, 4498–4506.
144 L. Frouté, K. M. Guan, W. Yun, S. J. Y. Lewis, B. D. Stripe, X. Yang, A. Lapene, A. R. Kovscek and P. Creux, *Lab Chip*, 2023, **23**, 3978–3988.
145 S. Morais, C. Lecoutre, G. Philippot, G. Aubert, O. Nguyen, A. Cario, E. Vidal, Z. Campbell, Y. Garrabos, M. Azaroual, L. Helfen, D. Bernard and S. Marre, *Processes*, 2023, **11**, 1981.
146 A. Chaudhury, A. Pantazis and N. Chronis, *Sens. Actuators, A*, 2016, **245**, 63–67.
147 I. M. Zarikos, S. M. Hassanizadeh, L. M. van Oosterhout and W. van Oordt, *Transp. Porous Media*, 2018, **122**, 221–234.
148 M. Abkarian, M. Faivre and H. A. Stone, *Proc. Natl. Acad. Sci. U. S. A.*, 2006, **103**, 538–542.
149 F. Shen, M. Ai, J. Ma, Z. Li and S. Xue, *Micromachines*, 2020, **11**, 914.
150 N. Raventhiran, R. S. Molla, K. Nandishwara, E. Johnson and Y. Li, *Lab Chip*, 2022, **22**, 4306–4316.
151 M. Sesen and W. Graeme, *Sci. Rep.*, 2020, **10**, 8736.
152 J. Riti, G. Sutra, T. Naas, H. Volland, S. Simon and K. Perez-Toralla, *Biosens. Bioelectron.*, 2024, **257**, 116301.
153 W. Haiyi, F. Wen-Zhen, K. Qinjun, T. Wen-Quan and Q. Rui, *Sci. Rep.*, 2019, **9**, 20387.
154 W. Yun, Y. Liu and A. R. Kovscek, *Adv. Water Resour.*, 2020, **144**, 103708.
155 N. I. Prasianakis, R. Haller, M. Mahrous, J. Poonoosamy, W. Pfingsten and S. V. Churakov, *Geochim. Cosmochim. Acta*, 2020, **291**, 126–143.